









Square and rhombic lattices of magnetic skyrmions in a centrosymmetric binary compound

Rina Takagi ^{1,2,3,4✉}, Naofumi Matsuyama¹, Victor Ukleev⁵, Le Yu^{5,6,7}, Jonathan S. White ⁵, Sonia Francoual ⁸, José R. L. Mardegan⁸, Satoru Hayami ^{1,3}, Hiraku Saito⁹, Koji Kaneko^{10,11}, Kazuki Ohishi ¹², Yoshichika Ōnuki⁴, Taka-hisa Arima ^{4,13}, Yoshinori Tokura ^{1,4,14}, Taro Nakajima ^{4,9} & Shinichiro Seki^{1,2,3,4}

Magnetic skyrmions are topologically stable swirling spin textures with particle-like character, and have been intensively studied as a candidate of high-density information bit. While magnetic skyrmions were originally discovered in noncentrosymmetric systems with Dzyaloshinskii-Moriya interaction, recently a nanometric skyrmion lattice has also been reported for centrosymmetric rare-earth compounds, such as Gd_2PdSi_3 and GdRu_2Si_2 . For the latter systems, a distinct skyrmion formation mechanism mediated by itinerant electrons has been proposed, and the search of a simpler model system allowing for a better understanding of their intricate magnetic phase diagram is highly demanded. Here, we report the discovery of square and rhombic lattices of nanometric skyrmions in a centrosymmetric binary compound EuAl_4 , by performing small-angle neutron and resonant elastic X-ray scattering experiments. Unlike previously reported centrosymmetric skyrmion-hosting materials, EuAl_4 shows multiple-step reorientation of the fundamental magnetic modulation vector as a function of magnetic field, probably reflecting a delicate balance of associated itinerant-electron-mediated interactions. The present results demonstrate that a variety of distinctive skyrmion orders can be derived even in a simple centrosymmetric binary compound, which highlights rare-earth intermetallic systems as a promising platform to realize/control the competition of multiple topological magnetic phases in a single material.

¹Department of Applied Physics, University of Tokyo, Tokyo 113-8656, Japan. ²Institute of Engineering Innovation, University of Tokyo, Tokyo 113-0032, Japan. ³PRESTO, Japan Science and Technology Agency (JST), Kawaguchi 332-0012, Japan. ⁴RIKEN Center for Emergent Matter Science (CEMS), Wako 351-0198, Japan. ⁵Laboratory for Neutron Scattering and Imaging (LNS), Paul Scherrer Institute (PSI), 5232 Villigen, Switzerland. ⁶Laboratory for Ultrafast Microscopy and Electron Scattering (LUMES), Institute of Physics, École Polytechnique Fédérale de Lausanne (EPFL), 1015 Lausanne, Switzerland. ⁷Laboratory of Nanoscale Magnetic Materials and Magnonics (LMGN), Institute of Materials, École Polytechnique Fédérale de Lausanne (EPFL), 1015 Lausanne, Switzerland. ⁸Deutsches Elektronen-Synchrotron DESY, Notkestraße 85, 22607 Hamburg, Germany. ⁹The Institute for Solid State Physics, University of Tokyo, Kashiwa 277-8561, Japan. ¹⁰Materials Sciences Research Center, Japan Atomic Energy Agency, Tokai 319-1195, Japan. ¹¹J-PARC Center, Japan Atomic Energy Agency, Tokai 319-1195, Japan. ¹²Neutron Science and Technology Center, Comprehensive Research Organization for Science and Society (CROSS), Tokai 319-1106, Japan. ¹³Department of Advanced Materials Science, University of Tokyo, Kashiwa 277-8561, Japan. ¹⁴Tokyo College, University of Tokyo, Tokyo 113-8656, Japan. ✉email: takagi@ap.t.u-tokyo.ac.jp

Recently, the concept of topology is attracting attention as a source for various exotic phenomena in solids. One typical example is magnetic skyrmion, i.e., a noncoplanar swirling spin structure with topologically stable particle-like nature (Fig. 1c). It is characterized by non-zero integer skyrmion number N_{sk} defined as:

$$N_{\text{sk}} = \frac{1}{4\pi} \int \mathbf{n} \cdot \left(\frac{\partial \mathbf{n}}{\partial x} \times \frac{\partial \mathbf{n}}{\partial y} \right) dx dy \quad (1)$$

with $\mathbf{n}(\mathbf{r}) = \mathbf{m}(\mathbf{r})/|\mathbf{m}(\mathbf{r})|$ being the unit vector along the direction of local magnetic moment $\mathbf{m}(\mathbf{r})$, which represents how many times $\mathbf{n}(\mathbf{r})$ wrap a sphere¹. In metallic compounds, skyrmion spin textures induce fictitious magnetic fluxes acting on the conduction electrons through quantum-mechanical Berry phase, which leads to various exotic transport phenomena, such as the topological Hall effect^{2–4}. Conversely, an applied electric current can efficiently drive the skyrmion motion through a spin transfer torque, whose threshold current density is often five orders of magnitude smaller than for conventional ferromagnetic domain walls^{3,4}. These features highlight skyrmions as potential novel information carriers with high-energy efficiency and information density.

Previously, magnetic skyrmions were mostly observed in noncentrosymmetric systems, where a competition between the ferromagnetic exchange and Dzyaloshinskii-Moriya (DM) interactions stabilizes a triangular skyrmion lattice (SkL) state^{1,5–15}. On the other hand, a SkL has recently been discovered for centrosymmetric rare-earth-based compounds. In the latter systems, the symmetry of the SkL usually reflects that of the underlying crystal lattice, such as triangular SkL in hexagonal Gd_2PdSi_3 and $\text{Gd}_3\text{Ru}_4\text{Al}_{12}$ and square SkL in tetragonal GdRu_2Si_2 ^{16–18}. Notably,

these centrosymmetric materials commonly host extremely small skyrmions of diameter less than 5 nm, which is almost one order of magnitude smaller than the typical skyrmion diameter in conventional DM-based bulk magnets. For such systems, a distinct skyrmion formation mechanism mediated by itinerant electrons has been proposed^{19–22}, and this theoretical framework successfully explains the magnetic phase diagram and the associated spin-charge coupling in GdRu_2Si_2 ^{17,23}. To date, the examples of skyrmion-hosting centrosymmetric magnets are limited to a few Gd-based intermetallics, and further search of simpler model compounds and better understanding of their intricate magnetic phase diagram are highly demanded.

In this work, we focus on a simple centrosymmetric binary compound EuAl_4 , and investigate its magnetic structure by means of neutron and X-ray scattering experiments. Unlike previously reported systems, EuAl_4 turns out to host two distinctive topological magnetic phases, i.e., a square and a rhombic lattice state of skyrmions with a diameter of 3.5 nm, which is accompanied by the multiple-step reorientation of fundamental magnetic modulation vector as a function of magnetic field. The present results highlight EuAl_4 as the simple model system to embody the unique itinerant-electron-mediated skyrmion formation mechanism, and suggest that a similar competition among multiple topological magnetic phases can be widely expected in other rare-earth-based intermetallic systems.

Results

Our target material EuAl_4 has the centrosymmetric tetragonal crystal structure, which belongs to the space group $I4/mmm$ (No. 139) as shown in Fig. 1a²⁴. This compound is reported to form a charge density wave characterized by the incommensurate

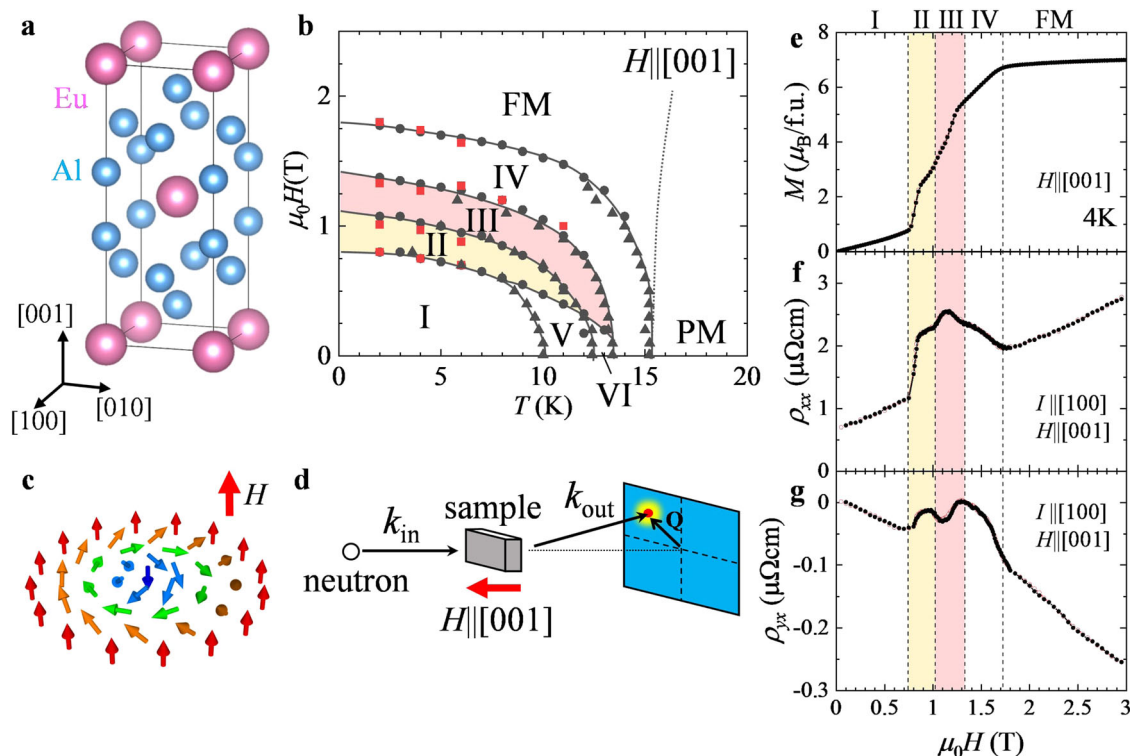


Fig. 1 Magnetic phase diagram of EuAl_4 . **a** Crystal structure of EuAl_4 . **b** H (magnetic field)- T (temperature) phase diagram for $H \parallel [001]$ determined from T and H dependences of magnetization, M (black triangular and circle symbols, respectively), and the H dependence of Hall resistivity, ρ_{yx} (red square symbols). FM and PM represent the ferromagnetic and paramagnetic states, respectively. **c** Schematic illustration of the skyrmion spin texture. **d** Schematic illustration of the experimental geometry for the SANS measurement. k_{in} and k_{out} are the incident and scattered neutron wave vectors, respectively. **e-g** Magnetic-field dependence of magnetization M (**e**), longitudinal resistivity ρ_{xx} (**f**), and Hall resistivity ρ_{yx} (**g**) at 4 K for $H \parallel [001]$ and $I \parallel [100]$. Black filled and red open circles correspond to the field-increasing and -decreasing processes, respectively.

ordering vector along the [001] axis below 145 K²⁵ (See Supplementary Note X for the detailed discussion on the charge density wave and crystal symmetry). The magnetism is governed by the Eu²⁺ ($S = 7/2$, $L = 0$) ions with Heisenberg magnetic moment, and the square lattice layers of Eu²⁺ and nonmagnetic Al layers are alternately stacked along the [001] axis. According to the previous neutron scattering experiment under zero magnetic field, this compound hosts incommensurate magnetic orders below $T_N = 15.4$ K²⁶. It is characterized by the weak easy-axis magnetic anisotropy, and shows multiple-step metamagnetic transitions as sweeping the external magnetic field $\mathbf{H} \parallel [001]$ ²⁴. Very recently, the non-monotonous H -dependence of Hall resistivity was reported, and its possible relevance to topological Hall effect was discussed²⁷. At this stage, the magnetic structure for each phase in magnetic fields has not been identified experimentally.

First, we investigated the magnetic phase diagram of EuAl₄ for $\mathbf{H} \parallel [001]$. Figure 1e–g shows the H -dependence of magnetization M , resistivity ρ_{xx} , and Hall resistivity ρ_{yx} measured at 4 K for $\mathbf{H} \parallel [001]$ and $\mathbf{I} \parallel [100]$, respectively. The magnetization curves show multiple-step metamagnetic transitions before reaching the forced ferromagnetic (FM) state, which is accompanied by non-monotonous changes in ρ_{xx} and ρ_{yx} . These behaviors are in agreement with previous reports^{24,27} (See Supplementary Note V for the detailed interpretation of ρ_{yx} profile). By performing similar measurements at selected temperatures, the H - T (temperature) magnetic phase diagram is summarized in Fig. 1b. Below 8 K, four distinctive magnetic phases (i.e., phases I, II, III, and IV) are identified. The H -values for the anomalies observed in the M , ρ_{xx} and ρ_{yx} profiles coincide with each other, which suggests a strong coupling between the magnetism and the electrical transport properties.

Next, in order to identify the magnetic modulation vector in each phase, a series of small-angle neutron scattering (SANS) experiments for the (001) plane at 5.0 K in $\mathbf{H} \parallel [001]$ of various strengths were performed. Here, both the direction of the incident neutron beam and that of the external magnetic field are parallel to the [001] direction, as shown in Fig. 1d. When the Fourier transform of magnetic structure contains the modulated spin component ($\hat{\mathbf{m}}(\mathbf{Q})\exp[i\mathbf{Q}\cdot\mathbf{r}] + \text{c.c.}$) with $\hat{\mathbf{m}}(\mathbf{Q})$ being a complex vector and c.c. representing complex conjugate, SANS is generally sensitive to the component of $\hat{\mathbf{m}}(\mathbf{Q})$ normal to the magnetic modulation vector \mathbf{Q} ²⁸. Figure 2a–d shows the typical SANS patterns obtained in phases I, II, III and IV, respectively. Here, we define θ_Q as the angle between the \mathbf{Q} -vector and the [110] axis, and \mathbf{Q}_1 as the direction of fundamental magnetic modulation vector. In phase I at $H = 0$ (Fig. 2a), we observed magnetic reflections at $\mathbf{Q} = \mathbf{Q}_1$ along the $\langle 100 \rangle$ directions (i.e. $\theta_Q \sim 45^\circ$). By increasing the magnetic field, the \mathbf{Q}_1 -direction switches to $\theta_Q \sim \pm 5^\circ$ upon entering phase II (Fig. 2b), and is further aligned along the $\langle 110 \rangle$ direction in phase III (i.e. $\theta_Q \sim 0^\circ$) (Fig. 2c). At higher fields, the \mathbf{Q}_1 -direction is tilted back to $\theta_Q \sim \pm 5^\circ$ in phase IV (Fig. 2d). Figure 3e, f exhibits the magnetic-field variations of the wavenumber $|Q|$ and the azimuth angle θ_Q for the fundamental magnetic reflection $\mathbf{Q} = \mathbf{Q}_1$, respectively. θ_Q takes distinctive values in each phase, demonstrating the multiple-step reorientation of the fundamental modulation vector in this compound. In phase I, $|Q|$ is almost constant at around 0.28 \AA^{-1} , which corresponds to a modulation period of 2.2 nm. In phases II–IV, $|Q|$ is around 0.18 \AA^{-1} giving a modulation period of 3.5 nm. Note that the observed fundamental modulation vector \mathbf{Q}_1 is always incommensurate, i.e. $\mathbf{Q}_1 \sim (0, 0.19, 0)$, $(0.073, 0.097, 0)$, $(0.083, 0.083, 0)$, and $(0.070, 0.092, 0)$ in phases I, II, III, and IV, respectively. Here, reflecting the tetragonal symmetry of the underlying crystal lattice, multiple equivalent magnetic reflections are observed in the SANS pattern for each phase. In phase III, for

instance, four fundamental magnetic reflections corresponding to $\mathbf{Q}_1 = (q, q, 0)$, $\mathbf{Q}_2 = (q, -q, 0)$ as well as $-\mathbf{Q}_1$ and $-\mathbf{Q}_2$ are identified (Fig. 2c). Such scattering patterns can originate from a multiple- Q spin order hosting multiple number of modulation vectors, or the spatial coexistence of symmetrically equivalent magnetic domains that are related by symmetry elements lost during the phase transition. One straightforward method to distinguish between these two possibilities is the detection of intensity at the $\mathbf{Q}_1 + \mathbf{Q}_2$ position, which should appear only in the multiple- Q state^{17,29,30}. Remarkably, we have identified the clear $\mathbf{Q}_1 + \mathbf{Q}_2$ reflection in phases II and III (Fig. 2b, c), demonstrating that phases II and III are double- Q states. Figure 3g, h indicates the magnetic-field dependence of the wavenumber $|Q|$ and the azimuth angle θ_Q for the $\mathbf{Q}_1 + \mathbf{Q}_2$ position. The experimentally observed $|Q|$ and θ_Q values for the $\mathbf{Q}_1 + \mathbf{Q}_2$ reflections are consistent with the ones expected from the fundamental reflections (solid lines in Fig. 3g, h). As detailed in Supplementary Notes I, II, and III, similar $\mathbf{Q}_1 + \mathbf{Q}_2$ (as well as the associated $\mathbf{Q}_1 - \mathbf{Q}_2$) reflections have been identified in the resonant X-ray scattering experiments characterized by better momentum-space resolution. Note that in phase II, the \mathbf{Q}_1 and \mathbf{Q}_2 directions are not orthogonal to each other, and therefore two double- Q states related by the lost four-fold symmetry can coexist as detailed in Supplementary Note II. This explains the observed appearance of eight fundamental reflection spots in phase II (Fig. 2b). By considering a similar magnetic domain formation, the scattering patterns in phases I and IV can be also reasonably explained.

Figure 3c, d exhibits the magnetic-field variations of the SANS integrated intensities measured for Area 1 and Area 2, i.e., the boxed regions along the $\langle 100 \rangle$ and $\langle 110 \rangle$ directions as indicated in Fig. 3a, b, respectively. In phase I with $\mathbf{Q}_1 \parallel \langle 100 \rangle$, the SANS intensity is observed only in Area 1. In phases II, III and IV, the SANS intensity emerges in Area 2, reflecting the reorientation of fundamental magnetic modulation vector \mathbf{Q}_1 . In phases II and III, finite SANS intensity is also observed in Area 1, which corresponds to the $\mathbf{Q}_1 + \mathbf{Q}_2$ reflections originating from the double- Q nature of these phases.

To investigate the detailed spin orientations in each phase, we have further performed polarized SANS measurements with the experimental setup shown in Fig. 4a. Here, the neutron spin orientation \mathbf{S}_n is aligned parallel or antiparallel to the incident neutron beam ($\parallel [001]$), and the intensities of spin-flip and non-spin-flip scattering (I_{SF} and I_{NSF} , respectively) are measured separately (Fig. 4a). In this configuration, I_{SF} reflects the component of $\hat{\mathbf{m}}(\mathbf{Q})$ normal to both $\mathbf{S}_n \parallel [001]$ and \mathbf{Q} , and I_{NSF} reflects the component of $\hat{\mathbf{m}}(\mathbf{Q})$ parallel to $\mathbf{S}_n \parallel [001]$ (Fig. 4b)²⁸. To access phases II, III and IV, temperature was swept with $\mu_0 H = 1$ T applied along the [001] direction. In Fig. 4f–i, the line-scan profiles of I_{SF} and I_{NSF} are plotted for the fundamental magnetic reflections in phases II and III. The corresponding line-scan direction in the reciprocal space is presented in Fig. 4d, e. Magnetic reflections are observed for both I_{SF} and I_{NSF} channels, which proves that $\hat{\mathbf{m}}(\mathbf{Q})$ possesses both in-plane and out-of-plane components normal to \mathbf{Q} . This result suggests that $\hat{\mathbf{m}}(\mathbf{Q})$ in phases II and III are characterized by the screw-type spin modulation (Fig. 4b), where their neighboring spins rotate within a plane normal to the magnetic modulation vector \mathbf{Q} . By considering the double- Q nature of phases II and III, their spin textures $\mathbf{m}(\mathbf{r}) = \mathbf{s}(\mathbf{r})/|\mathbf{s}(\mathbf{r})|$ should be approximately described as

$$\mathbf{s}(\mathbf{r}) = s_0^z + \sum_{i=1,2} \left(s_{Q_i}^{xy} \cos(\mathbf{Q}_i \cdot \mathbf{r}) + s_0^z \sin(\mathbf{Q}_i \cdot \mathbf{r}) \right) \quad (2)$$

which represents the superposition of screw spin helices characterized by two obliquely or orthogonally arranged magnetic modulation vectors \mathbf{Q}_1 and \mathbf{Q}_2 , respectively. s_0^z is the H -induced uniform magnetization component along the [001] axis, and $s_{Q_i}^{xy}$

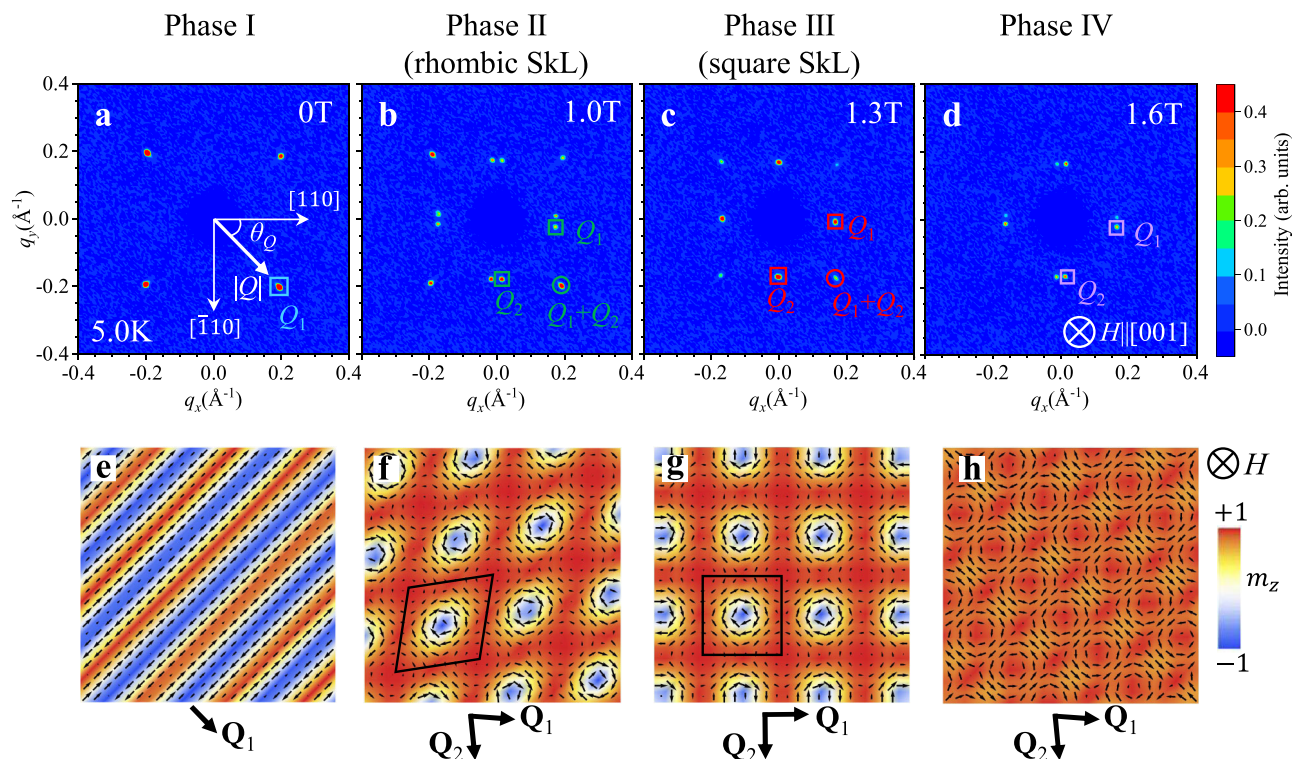


Fig. 2 Magnetic-field dependence of SANS patterns for EuAl_4 . **a-d** Typical SANS patterns taken at 5.0 K at various strengths of magnetic field for $H \parallel [001]$. The color scale indicates the integrated intensity. **e-h** Schematics of the screw (**e**), rhombic skyrmion lattice (**f**), square skyrmion lattice (**g**), and vortex-lattice (**h**) spin textures. Each phase is characterized by distinctive orientation of the fundamental magnetic modulation vectors \mathbf{Q}_1 and \mathbf{Q}_2 . The rhombic and square skyrmion lattice states are the double-Q states described by Eq. (2), i.e., the superposition of two obliquely or orthogonally modulated spin helices. Background color represents the out-of-plane component of local magnetic moment m_z . See Supplementary Note VII and VIII for the detailed spin texture in phase IV.

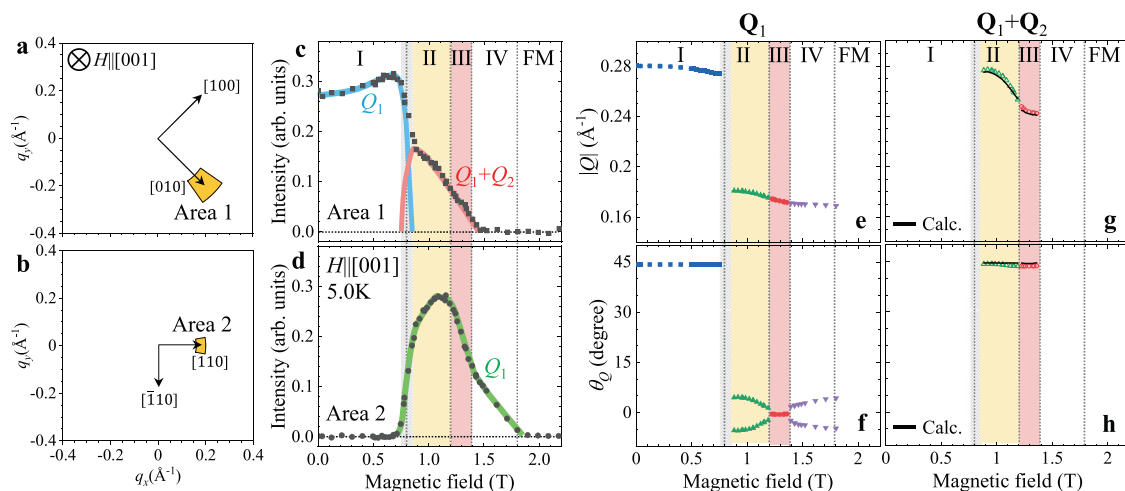


Fig. 3 Magnetic-field dependence of the magnetic modulation vectors in EuAl_4 . **a, b** Schematic illustrations of Area 1 and Area 2 used for the SANS intensity integration. **c, d** The SANS integrated intensities for Area 1 (**a**) and Area 2 (**b**) as a function of magnetic field for $H \parallel [001]$ at 5.0 K. The colored lines in (**c, d**) are guides to the eye, showing the assignment of each magnetic reflection to either \mathbf{Q}_1 or $\mathbf{Q}_1 + \mathbf{Q}_2$. **e, f** Magnetic-field dependence of the wavenumber $|\mathbf{Q}|$ (**e**) and azimuth angle θ_Q (**f**) of the fundamental magnetic modulation vector \mathbf{Q}_1 . Here, θ_Q is defined as the angle between the \mathbf{Q} -direction and the $[110]$ axis, as shown in Fig. 2a. **g, h** The corresponding data for the higher-order $\mathbf{Q}_1 + \mathbf{Q}_2$ magnetic satellite reflection. The black curves in (**g, h**) represent the theoretical $|\mathbf{Q}|$ and θ_Q values for $\mathbf{Q}_1 + \mathbf{Q}_2$ reflection calculated from fundamental magnetic reflections in (**e, f**), which agree well with the experimental data. The gray regions between phases I and II indicate the phase coexistence region (see Supplementary Note IV).

($s_{\mathbf{Q}}^z$) represents the modulated spin component normal to both magnetic modulation vector \mathbf{Q} , and the $[001]$ axis (parallel to the $[001]$ axis). The resultant spin textures for phases II and III are illustrated in Fig. 2f, g, which can be considered as the rhombic and square lattice of magnetic skyrmions, respectively, according

to Eq. (1). In Fig. 4c, the temperature dependence of I_{SF} and I_{NSF} measured at 1 T is summarized. In phase IV above 11 K, the magnetic scattering appears only in the I_{SF} channel but not in the I_{NSF} channel. It suggests that $\hat{\mathbf{m}}(\mathbf{Q})$ in phase IV consists only of the in-plane component normal to \mathbf{Q} . A similar conclusion is also

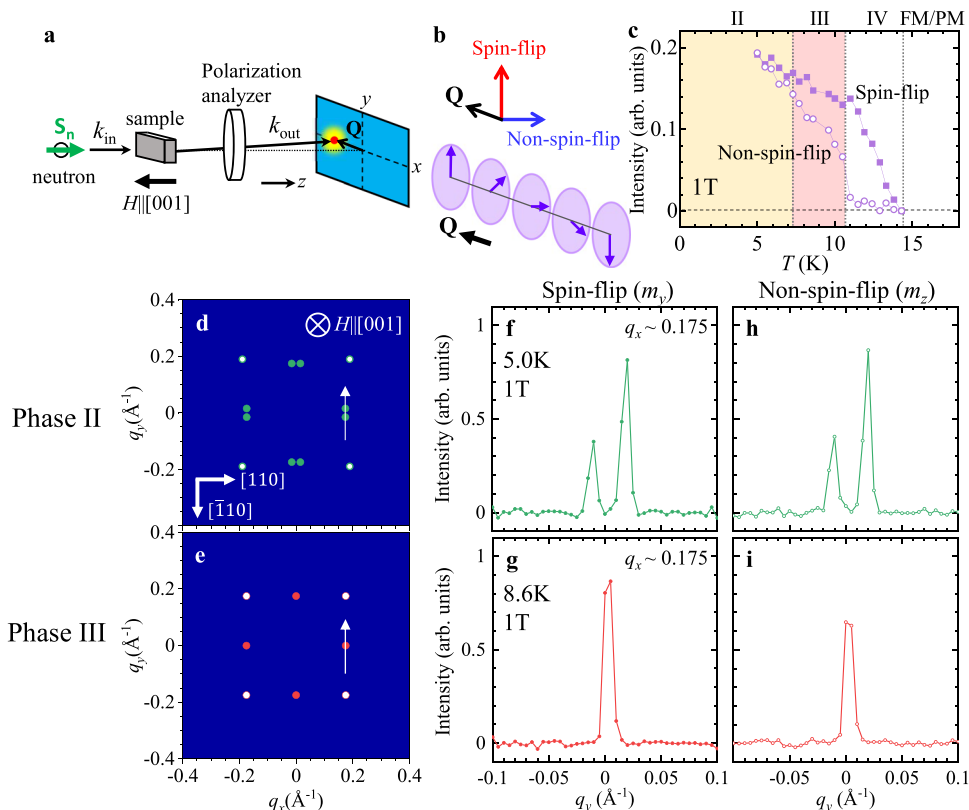


Fig. 4 Polarized SANS study of the modulated magnetic states. **a, b** Schematic illustration of **(a)** experimental setup and **(b)** the magnetic scattering selection rules. \mathbf{S}_n represents the direction of the neutron polarization, which is aligned parallel or antiparallel with $\mathbf{k}_{in} \parallel [001]$. Only a modulated spin component $\hat{\mathbf{m}}(\mathbf{Q})$ normal to \mathbf{Q} can give rise to magnetic neutron scattering. In this setup, spin-flip (SF) scattering arises due to the in-plane component of $\hat{\mathbf{m}}(\mathbf{Q})$ perpendicular to both \mathbf{Q} and $\mathbf{S}_n \parallel [001]$ (red arrow), and non-spin-flip (NSF) scattering arises due to the out-of-plane component of $\hat{\mathbf{m}}(\mathbf{Q})$ parallel to $\mathbf{S}_n \parallel [001]$ (blue arrow). **c** Temperature variations of the scattering intensity of SF and NSF channels at 1 T. **d, e** Schematic illustration of SANS patterns for phases II and III. The arrows indicate the line-scan directions of **(f–i)**. **f–i** Line-scan profiles for **(f, g)** spin-flip and **(h, i)** non-spin-flip channels measured in phases II and III at 1 T, which detect in-plane and out-of-plane component of $\hat{\mathbf{m}}(\mathbf{Q})$ (i.e. $\hat{m}_y(\mathbf{Q})$ and $\hat{m}_z(\mathbf{Q})$), respectively. Here, the scattering intensity is integrated for the range of $q_x = 0.175 \pm 0.005 \text{ \AA}^{-1}$. The asymmetry of two peak intensities in phase II **(f, h)** is probably due to different populations of the two equivalent magnetic domains.

obtained from the resonant elastic X-ray scattering results for phase IV, as discussed in Supplementary Note I. Note that additional neutron scattering data in Supplementary Fig. 8 indicate the existence of very weak but discernible $\mathbf{Q}_1 + \mathbf{Q}_2$ reflection in phase IV, which suggests the formation of double-Q vortex-lattice spin state described by the superposition of two sinusoidally-modulated in-plane spin components (Fig. 2h). For the detailed discussion on the spin texture for phase IV, see Supplementary Note VII and VIII.

Discussion

In the following, we discuss the microscopic origin for the appearance of square and rhombic SkL states in EuAl_4 . Since the crystal structure of EuAl_4 is centrosymmetric, the contribution of DM interaction should be absent and some different mechanism must be considered. According to the recent theoretical studies^{19–22}, the SkL formation in centrosymmetric rare-earth compounds are approximately explained by the combination of Ruderman-Kittel-Kasuya-Yosida (RKKY) interaction $\hat{J}(\mathbf{Q})[\hat{\mathbf{m}}(\mathbf{Q}) \cdot \hat{\mathbf{m}}(-\mathbf{Q})]$ and four-spin interaction $\hat{K}(\mathbf{Q})[\hat{\mathbf{m}}(\mathbf{Q}) \cdot \hat{\mathbf{m}}(-\mathbf{Q})]^2$, which are derived from the Kondo lattice model consisting of localized magnetic moments and itinerant electrons. Here, the former RKKY term stabilizes the magnetic modulation with a specific wave vector, and the latter four-spin interaction term enhances the stability of the multiple-Q orders.

This model well explains the recently reported square SkL formation in a centrosymmetric tetragonal magnet GdRu_2Si_2 ^{17,23}, and similar mechanism would be also relevant for EuAl_4 having the same tetragonal crystal structure.

Compared to the known skyrmion-hosting materials, the present EuAl_4 is characterized by several unique features. First, EuAl_4 shows multiple-step reorientation of the fundamental magnetic modulation vector as a function of external magnetic field, which leads to the appearance of not only square, but also rhombic form of SkL states. These behaviors are distinctive from the previously reported centrosymmetric Gd-compounds^{16–18}, where the magnetic modulation vector is always fixed along the one specific direction and the associated SkL reflects the symmetry of underlying crystal lattice. (For example, only the square SkL appears for tetragonal GdRu_2Si_2 with $\mathbf{Q} \parallel \langle 100 \rangle$ ¹⁷). In general, the orientation and length of stable magnetic modulation vector are determined by the peak position in $\hat{J}(\mathbf{Q})$ reflecting the character of the associated Fermi surfaces or electronic structure. The presently observed multiple-step \mathbf{Q} -reorientation in EuAl_4 implies that almost comparable amplitude of $\hat{J}(\mathbf{Q})$ peaks exist for several \mathbf{Q} -positions. In Supplementary Note IX and Supplementary Fig. 10, we performed theoretical simulation based on this assumption, which turned out to well reproduce the observed H -induced transition between rhombic and square SkL states. This suggests that the symmetry of SkL sensitively depends on the

electronic structure²⁰ and potentially can be controlled by chemical substitution or external stimuli, which would be a unique feature of itinerant-electron-mediated mechanism compared with the traditional DM-based mechanism.

Second, EuAl_4 is the first example of centrosymmetric binary compound to host skyrmion spin texture, which just consists of the alternate stacking of magnetic Eu layer and non-magnetic Al layer (Fig. 1a). The interactions among the Eu^{2+} localized magnetic moments are mediated by itinerant electrons, whose Fermi surfaces are mostly governed by Al according to the recent ARPES (angle-resolved photoemission spectroscopy) measurements³¹. The above features highlight EuAl_4 as the simple model system to embody the unique skyrmion formation mechanisms mediated by itinerant electrons. It is remarkable that even such a minimum centrosymmetric binary compound can host a variety of distinctive skyrmion orders with intricate multiple-step Q-reorientation. The present experimental results demonstrate that rare-earth intermetallics with delicate balance of magnetic interactions^{19–22,32–36} can be a promising platform to realize/control the competition of multiple topological magnetic phases in a single compound, which would be a good guideline for further search of exotic materials with emergent functional responses.

Methods

Sample preparation and characterization. Single crystals of EuAl_4 were grown by the Al self-flux method. The samples were characterized by powder X-ray diffraction, which confirmed the purity of the grown crystals. Crystal orientations were determined by Laue X-ray diffraction, and then the samples were cut out from the crystal with a wire saw and carefully mechanically polished.

Magnetization and resistivity measurements. Magnetization was measured using a SQUID magnetometer (Magnetic Property Measurement System, Quantum Design). The longitudinal (ρ_{xx}) and Hall (ρ_{yx}) resistivities were measured using the ac-transport option in a physical property measurement system (PPMS, Quantum Design). Measurements of magnetic and electrical transport properties were performed on the same crystal with a dimension of 1 mm by 0.9 mm by 0.5 mm.

SANS measurements. SANS measurements were carried out at the time-of-flight type small-and-wide-angle neutron scattering instrument TAIKAN (BL15) at Materials and Life Science Experimental Facility (MLF) in Japan Proton Accelerator Research Complex (J-PARC)³⁷. A thin crystal with a thickness of 0.2 mm having the widest surface of 5 mm by 2.5 mm parallel to the (001) plane was installed in a cryostat equipped with a horizontal-field superconducting magnet. An incident neutron beam with a wavelength ranging from 0.7 to 7.7 Å was exposed on the sample. The incident beam was always directed along the [001] axis within the accuracy of 2 degrees. The typical measuring time for a SANS pattern was 200 s. The SANS patterns (Fig. 2) were measured with rotating and tilting the sample up to 2 degrees. Background data were obtained at 15.5 K above T_c in a magnetic field of 0.05 T, and subtracted from the data obtained at low T to leave only the magnetic signal. As for the magnetic-field scans, SANS signals were collected with continuously increasing magnetic field at a sweeping rate of 0.01 T/min.

In the SANS experiments with longitudinal polarization analysis, a polarized incident neutron beam was obtained by a supermirror polarizer. The neutron spin polarization at the sample position was controlled to be parallel to the [001] axis of the sample by guide fields and the horizontal-field superconducting magnet, which applied a magnetic field of 1.0 T. A supermirror spin analyzer was set between the sample and the detectors, and was used to separate the spin-flip (SF) and non-spin-flip (NSF) scattering signals. Total beam polarization measured using a direct beam was 0.85 for the neutrons with the wavelengths longer than 3.5 Å. The incident and scattering angles for the fundamental magnetic Bragg reflections near the ($H, H, 0$) line were tuned so that the wavelengths for the Bragg reflections were approximately 3.5 Å. The mixing of the SF and NSF signals was corrected taking into account of the total beam polarization.

X-ray measurements. Resonant elastic X-ray scattering experiment was carried out using circularly polarized X-rays of an incoming photon energy tuned approximately to the Eu L_2 absorption edge (7617 eV) in Laue-transmission geometry on beamline P09 at the PETRA-III synchrotron, DESY. A (001)-oriented thin plate of EuAl_4 with a thickness of 10 μm and an area of 600 μm by 300 μm was attached to a Si_3N_4 substrate (almost X-ray transparent). The substrate was attached to a sample holder mounted at the bottom of a long probe and inserted into the variable temperature insert (VTI). The X-ray beam was focused to a spot

size of $\sim 70 \times 200 \mu\text{m}^2$. Diffraction patterns were recorded by a two-dimensional detector PILATUS300K by rocking the sample. A magnetic field was applied parallel to the incident X-ray beam and perpendicular to the thin plate (\parallel [001]) by a cryogen-free vector magnet. Background data were measured at 14.5 K where no magnetic scattering was observed.

Data availability

The data presented in this study are available from the corresponding author upon reasonable request.

Received: 24 June 2021; Accepted: 1 March 2022;

Published online: 30 March 2022

References

- Nagaosa, N. & Tokura, Y. Topological properties and dynamics of magnetic skyrmions. *Nat. Nanotech.* **8**, 899–911 (2013).
- Neubauer, A. et al. Topological Hall effect in the A phase of MnSi. *Phys. Rev. Lett.* **102**, 186602 (2009).
- Jonietz, F. et al. Spin transfer torques in MnSi at ultralow current densities. *Science* **330**, 1648–1651 (2010).
- Schulz, T. et al. Emergent electrodynamics of skyrmions in a chiral magnet. *Nat. Phys.* **8**, 301–304 (2012).
- Rößler, U. K., Bogdanov, A. N. & Pfléiderer, C. Spontaneous skyrmion ground states in magnetic metals. *Nature* **442**, 797–801 (2006).
- Mühlbauer, S. et al. Skyrmion lattice in a chiral magnet. *Science* **323**, 915–919 (2009).
- Yu, X. Z. et al. Real-space observation of a two-dimensional skyrmion crystal. *Nature* **465**, 901–904 (2010).
- Romming, N. et al. Writing and deleting single magnetic skyrmions. *Science* **341**, 636–639 (2013).
- Fert, A., Cros, V. & Sampaio, J. Skyrmions on the track. *Nat. Nanotech.* **8**, 152–156 (2013).
- Fert, A., Reyren, N. & Cros, V. Magnetic skyrmions: advances in physics and potential applications. *Nat. Rev. Mater.* **2**, 17031 (2017).
- Bogdanov, A. & Hubert, A. Thermodynamically stable magnetic vortex states in magnetic crystals. *J. Mag. Mag. Mater.* **138**, 255–269 (1994).
- Seki, S., Yu, X. Z., Ishiwata, S. & Tokura, Y. Observation of skyrmions in a multiferroic material. *Science* **336**, 198–201 (2012).
- Tokunaga, Y. et al. A new class of chiral materials hosting magnetic skyrmions beyond room temperature. *Nat. Commun.* **6**, 7638–7644 (2015).
- Kézsmárki, I. et al. Néel-type skyrmion lattice with confined orientation in the polar magnetic semiconductor GaV_4S_8 . *Nat. Mater.* **14**, 1116–1122 (2015).
- Nayak, A. K. et al. Magnetic antiskyrmions above room temperature in tetragonal Heusler materials. *Nature* **548**, 561–566 (2017).
- Kurumaji, T. et al. Skyrmion lattice with a giant topological Hall effect in a frustrated triangular-lattice magnet. *Science* **365**, 914–918 (2019).
- Khanh, N. D. et al. Nanometric square skyrmion lattice in a centrosymmetric tetragonal magnet. *Nat. Nanotech.* **15**, 444–449 (2020).
- Hirschberger, M. et al. Skyrmion phase and competing magnetic orders on a breathing Kagomé lattice. *Nat. Commun.* **10**, 5831 (2019).
- Ozawa, R., Hayami, S. & Motome, Y. Zero-field skyrmions with a high topological number in itinerant magnets. *Phys. Rev. Lett.* **118**, 147205 (2017).
- Hayami, S., Ozawa, R. & Motome, Y. Effective bilinear-biquadratic model for noncoplanar ordering in itinerant magnets. *Phys. Rev. B* **95**, 224424 (2017).
- Wang, Z., Su, Y., Lin, S.-Z. & Batista, C. D. Skyrmion crystal from RKKY interaction mediated by 2D electron gas. *Phys. Rev. Lett.* **124**, 207201 (2020).
- Hayami, S. & Motome, Y. Square skyrmion crystal in centrosymmetric itinerant magnets. *Phys. Rev. B* **103**, 024439 (2021).
- Yasui, Y. et al. Imaging the coupling between itinerant electrons and localised moments in the centrosymmetric skyrmion magnet GdRu_2Si_2 . *Nat. Commun.* **11**, 5925 (2020).
- Nakamura, A. et al. Transport and magnetic properties of EuAl_4 and EuGa_4 . *J. Phys. Soc. Jpn.* **84**, 124711 (2015).
- Shimomura, S. et al. Lattice modulation and structural phase transition in the antiferromagnet EuAl_4 . *J. Phys. Soc. Jpn.* **88**, 014602 (2019).
- Kaneko, K. et al. Charge-density-wave order and multiple magnetic transitions in divalent europium compound EuAl_4 . *J. Phys. Soc. Jpn.* **90**, 064704 (2021).
- Shang, T. et al. Anomalous Hall resistivity and possible topological Hall effect in the EuAl_4 antiferromagnet. *Phys. Rev. B* **103**, L020405 (2021).
- Moon, R. M., Riste, T. & Koehler, W. C. Polarization analysis of thermal-neutron scattering. *Phys. Rev.* **181**, 920 (1969).
- Adams, T. et al. Long-range crystalline nature of the skyrmion lattice in MnSi. *Phys. Rev. Lett.* **107**, 217206 (2011).

30. Puphal, P. et al. Topological magnetic phase in the candidate Weyl semimetal CeAlGe. *Phys. Rev. Lett.* **124**, 017202 (2020).
31. Kobata, M. et al. Electronic structure of EuAl₄ studied by photoelectron spectroscopy. *J. Phys. Soc. Jpn.* **85**, 094703 (2016).
32. Okubo, T. et al. Multiple-*q* states and the Skyrmion lattice of the triangular-lattice heisenberg antiferromagnet under magnetic fields. *Phys. Rev. Lett.* **108**, 017206 (2012).
33. Leonov, A. O. & Mostovoy, M. Multiply periodic states and isolated skyrmions in an anisotropic frustrated magnet. *Nat. Commun.* **6**, 8275 (2015).
34. Wang, Z. et al. Meron, skyrmion, and vortex crystals in centrosymmetric tetragonal magnets. *Phys. Rev. B* **103**, 104408 (2021).
35. Martin, I. & Batista, C. D. Itinerant electron-driven chiral magnetic ordering and spontaneous quantum hall effect in triangular lattice models. *Phys. Rev. Lett.* **101**, 156402 (2008).
36. Utesov, O. I. Thermodynamically stable skyrmion lattice in a tetragonal frustrated antiferromagnet with dipolar interaction. *Phys. Rev. B* **103**, 064414 (2021).
37. Takata, S. et al. The design and *q* resolution of the small and wide angle neutron scattering instrument (TAIKAN) in J-PARC. *JPS Conf. Proc.* **8**, 036020 (2015).

Acknowledgements

The authors thank T. Shinohara, J. Bergtholdt, O. Leupold, P. J. Bereciartua, N. D. Khanh, X. Z. Yu, Y. Motome, T. Nomoto, R. Arita, M. Kriener, A. Kikkawa, and K. Nakajima for experimental support and valuable discussions. This work was partly supported by JSPS Grants-In-Aid for Scientific Research (Grants Nos. 17H02815, 18H03685, 19H01856, 20H00349, 20H01864, 21H04440, 21H04990, and 21K13876), PRESTO (Grant Nos. JPMJPR18L5, JPMJPR20B4, and JPMJPR20L8) and CREST (grant Nos. JPMJCR1874) from JST, Katsu Research Encouragement Award of the University of Tokyo, Asahi Glass Foundation, Murata Science Foundation, CALIPSOplus under the Grant Agreement 730872 from the EU Framework Programme for Research and Innovation HORIZON 2020, SNSF Sinergia CRSII5_171003 NanoSkyrmionics and SNSF Project No. 200021_188707. This work is based on experiments performed at Materials and Life Science Experimental Facility (MLF) in Japan Proton Accelerator Research Complex (J-PARC) (Proposal Nos. 2017L0701 and 2019C0006), Japan Research Reactor 3 (JRR-3) (Proposal Nos. 21512 and 21401) and PETRA-III at Deutsches Elektronen-Synchrotron (DESY), a Research Center of the Helmholtz Association (HGF), under proposal I-20190781 EC. The 6T/2T/2T superconducting vector magnet used for the experiment at P09 at PETRA-III was funded in part under Grant No. 05K2013 by the Bundesministerium für Bildung und Forschung. This work was partly performed using facilities of the Cryogenic Research Center, University of Tokyo.

Author contributions

R.T., S.S., V.U., J.S.W., T.N., T.A., and Y.T. conceived the project. R.T. and N.M. grew single crystals with the assistance of Y.O. R.T. and N.M. characterized the magnetic and transport properties. R.T., H.S., K.O., K.K., and T.N. performed neutron scattering measurements. R.T., V.U., L.Y., J.S.W., S.F., and J.R.L.M. performed resonant elastic X-ray scattering measurements. S.H. performed the theoretical simulation. R.T. and S.S. wrote the manuscript. The results were discussed and interpreted by all the authors.

Competing interests

The authors declare no competing interests.

Additional information

Supplementary information The online version contains supplementary material available at <https://doi.org/10.1038/s41467-022-29131-9>.

Correspondence and requests for materials should be addressed to Rina Takagi.

Peer review information *Nature Communications* thanks the anonymous reviewer(s) for their contribution to the peer review of this work.

Reprints and permission information is available at <http://www.nature.com/reprints>

Publisher's note Springer Nature remains neutral with regard to jurisdictional claims in published maps and institutional affiliations.



Open Access This article is licensed under a Creative Commons Attribution 4.0 International License, which permits use, sharing, adaptation, distribution and reproduction in any medium or format, as long as you give appropriate credit to the original author(s) and the source, provide a link to the Creative Commons license, and indicate if changes were made. The images or other third party material in this article are included in the article's Creative Commons license, unless indicated otherwise in a credit line to the material. If material is not included in the article's Creative Commons license and your intended use is not permitted by statutory regulation or exceeds the permitted use, you will need to obtain permission directly from the copyright holder. To view a copy of this license, visit <http://creativecommons.org/licenses/by/4.0/>.

© The Author(s) 2022